# Optical Properties and Orientation in Polyethylene Blown Films

AYUSH BAFNA,[1] GREGORY BEAUCAGE,[1] FRANCIS MIRABELLA,[2] GEORGE SKILLAS,[1] SATISH SUKUMARAN[1]

[1]Department of Material Science and Engineering, University of Cincinnati, Cincinnati, Ohio 45221-0012

[2]Technology Center, Equistar Chemicals, Cincinnati, Ohio 45249

*Received 30 April 2001; revised 5 September 2001; accepted 5 September 2001*

**ABSTRACT:** We report structural factors affecting the optical properties of blown polyethylene films. Two types of blown polyethylene films of similar degrees of crystallinity were made from (1) single-site-catalyst high-density polyethylene (HDPE; STAR $\alpha$) and (2) Ziegler–Natta-catalyst HDPE (ZN) resins. The STAR $\alpha$ film exhibited high clarity and gloss, whereas the ZN film was turbid. Small-angle X-ray scattering (SAXS), small-angle light scattering (SALS), and optical microscopy gave quantitative and qualitative information regarding structure and orientation in the films. A new approach is described for determining the three-dimensional lamellar normal orientation from SAXS. Both the clear STAR $\alpha$ and turbid ZN films had similar lamellar crystalline structures and long periods but displayed different degrees of orientation. It is demonstrated that optical haze is related to surface features that seem to be linked to the bulk morphology. The relationship between haze and structural orientation is described. The lamellar orientation is linked to rodlike structures seen in optical microscopy and SALS through a stacked lamellar or cylindrite morphology on a nanometer scale and through a fiberlike morphology on a micrometer scale. The micrometer-scale, rodlike structures seem directly related to surface roughness in a comparison of index-matched immersion and surface micrographs. The higher haze and lower gloss of the ZN film was caused by extensive surface roughness not observed in the STAR $\alpha$ film. © 2001 John Wiley & Sons, Inc. J Polym Sci Part B: Polym Phys 39: 2923–2936, 2001

**Keywords:** high-density polyethylene (HDPE); blown films; haze; three-dimensional (3D) orientation; SAXS; small-angle light scattering (SALS); optical microscopy

## INTRODUCTION

The optical properties of blown polyethylene films, including haze, gloss, transparency or clarity, and transmittance, are critical to end use. A fundamental understanding of the morphological basis for haze, for instance, is largely absent from the literature because the morphologies are complex, anisotropic, and generally not amenable to simple models. For blown polyethylene films, light scattering and reflection/refraction occur because of both bulk and surface structures.[1] Scattering takes place because of the presence of morphologies that may be related to the crystalline structure either in the bulk or on the surface of the polyethylene films.[1] The degree of scattering depends on the size of the crystalline structures present. If such crystalline structures exist on the scale of the wavelength of light, considerable diffuse reflection, refraction, and scattering occur, resulting in turbidity. Thus, the size and organi-

Contribution from the March 2001 Meeting of the American Physical Society–Division of Polymer Physics, Seattle, WA

*Correspondence to:* G. Beaucage (E-mail: gbeaucag@uceng.uc.edu)

Journal of Polymer Science: Part B: Polymer Physics, Vol. 39, 2923–2936 (2001)

zation of micrometer-scale crystalline structures plays an important role in deciding the optical properties of the films. In blown films, the morphologies tend to be oriented, and a relation between orientation, structure, and surface roughness may lead to an understanding of haze in blown films.

Several groups have reported on noncrystalline orientation with small-angle X-ray scattering (SAXS). Saw et al.[2] used SAXS for studying uniaxial crystalline orientation as a function of the drawing conditions of fibers and gave a detailed explanation of the generation of a fibrillar core in polyethylene terephthalate (PET) fibers by cold drawing. Murthy et al.[3] studied uniaxial lamellar orientation in fibers with SAXS. Prasad et al.[4] considered uniaxial orientation in blown films. They used SAXS for morphological studies and related the melt elasticity parameter $E_R$ to the lamellar orientation. Wilkes et al.[1] related the optical properties in blown polyethylene films to the surface structures. In various past publications,[5–7] the effect of morphology on the mechanical properties in blown polyethylene films has been studied. Jianjun and Hung-Jue[5] studied the effect of processing conditions on the morphology of films and related this to the dart impact resistance. Krishnaswamy and Sukhadai[6] characterized the orientation features of several linear low-density polyethylene (LLDPE) blown films and developed significant insight into the morphological origin of Elmendorf tear resistance. Yong-Man et al.[7] studied the effect of the length and distribution of short-chain branching on the mechanical properties of blown films of polyethylene.

Several authors have reported on the relationship between micrometer-scale structure and turbidity in blown films. Stehling et al.[8] reported the formation of rodlike superstructures on the surfaces of blown low-density polyethylene (LDPE) films. They related the surface roughness to the melt elasticity and showed that roughness increased as the melt elasticity increased; they also reported that decreasing the melt elasticity by mechanical degradation could decrease the haze. Hashimoto et al.[9] reported the formation of sheaflike superstructures on the surfaces of tubular extruded polybutune-1 films by electron microscopy. The sheaves were aligned side by side with the axis preferentially oriented perpendicular to the machine direction (MD), that is, the direction of stress. They concluded that the sheaflike structures caused light to scatter from the surfaces of the films. Kojima et al.[10] related the formation of irregularities on the inner and outer surfaces of high-density polyethylene (HDPE), LDPE, and LLDPE blown films to processing conditions and reported that these irregularities caused haziness in blown films. They showed that the degree of roughness depended on the rate of cooling of the films. Samuels[11] reported that rodlike, fibrillar structures (1–3 $\mu$m) formed on the surface of water-soluble hydroxypropylcellulose. These structures are reminiscent of those reported by Stehling et al.[8] Pinto and Larena[12] studied the light scattering from polyethylene tubular films and reported that the scattering was strongly correlated with the surface roughness. They showed that the degree of crystallinity played a secondary role in light scattering. They concluded that the degree of roughness decreased with (1) an increase in the extrusion temperature and (2) an increase in the melt index of the resin. The literature supports a dependence of the surface roughness on either the processing conditions or the properties of the resin, such as the melt index and melt elasticity. The nature of the crystalline structure and the degree of crystallinity have also been related to haze. Haudin et al.[13] characterized the unit cell orientation of the crystalline phase in LDPE films by three methods: Debye–Scherrer diagrams, pole figures, and orientation functions.

The two films reported in this article had similar processing conditions and degrees of crystallinity but showed different degrees of lamellar orientation. In this article, we attempt to relate the formation of irregularities on the surfaces of the films to the bulk morphology. The relation between haze and structural orientation is described with SAXS and small-angle light scattering (SALS). We develop a new approach to analyze the three-dimensional (3D) lamellar orientation in SAXS and correlate this to SALS and optical microscopy.

## EXPERIMENTAL

### Materials

Films designated ZN and STAR $\alpha$ were blown under similar conditions at Equistar Technology Center (Cincinnati OH) were studied. Two films with identical degrees of crystallinity (63% by differential scanning calorimetry and X-ray diffraction) are reported here. The ZN film was manufactured from HDPE synthesized with a

**Table I.** Molecular Weights and Haze Characteristics of the Polyethylenes and Films[a]

| Sample | $M_n$ (g/mol) | $M_w$ (g/mol) | MWD ($M_w/M_N$) | Haze (%) |
|---|---|---|---|---|
| STAR $\alpha$ | 10,780 | 46,090 | 4.28 | 16.3 |
| ZN | 12,400 | 176,560 | 14.24 | 60.0 |

[a] Haze was measured with ASTM D 103.

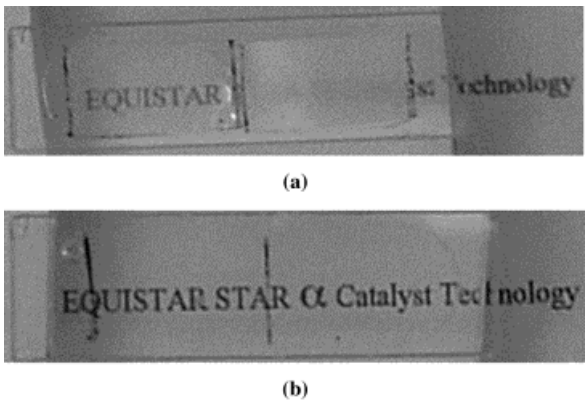


**Figure 1.** STAR $\alpha$ (left) and ZN (right) films, placed in cells 1.5 cm from the text, (a) held in air and (b) immersed in benzyl alcohol.

Ziegler–Natta third-generation titanium complex catalyst on an inorganic support, whereas the STAR $\alpha$ film was manufactured from HDPE synthesized with a single-site catalyst. The Ziegler–Natta catalyst gives HDPE with a broader molecular weight distribution (MWD) than that obtained from a single-site catalyst.[1] The molecular weights of the polymers [number-average molecular weight ($M_n$) and weight-average molecular weight ($M_w$)] are presented in Table I. The film processing conditions are presented in Table II. The ZN film was cloudy (60.0% haze), whereas the STAR $\alpha$ film was transparent (16.3% haze), as can be seen in Figure 1(a). Haze was measured on a BYK Gardner Haze-Gard Plus (ASTM D 103 test method). Both films were transparent on extrusion, but the ZN film turned hazy at a well-defined frost line.

## SAXS

### *SAXS Measurement*

SAXS measurements were conducted on a 2-m pinhole camera with focusing optics and a two-dimensional (2D) detector as described in earlier publications.[4,14] Data were corrected for dark current, empty cell, and sensitivity. The 2D measurements are useful in determining both lamellar nanostructure and orientation.

Because the films were very thin (50 $\mu$m); around 25–40 films were stacked over one another. Care was taken that the films were stacked in a such manner that all the films in a stack had their MD, transverse direction (TD), and normal direction (ND) aligned. Stacks around 1.25–1.50 mm thick were prepared from the 50-$\mu$m-thick films.

It is difficult to measure the component of orientation in the ND, that is, along the thickness of the film. This would require passing the X-ray beam in the plane of the film. We developed a simple approach with out-of-plane (M–T) tilts of $\phi_{Tilt}$ to access 3D orientation. This technique gives components of the degree of orientation in the MD, TD, and ND.

Figure 2 shows the three sample orientations used for the SAXS measurements:

1. M–T orientation: The sample was placed with the MD horizontal and TD vertical with the beam in the ND [Fig. 2(a)].
2. M–NT orientation: The sample, as in Figure 2(a), was rotated about the MD by 45° so that the orientation vector along the vertical axis was a combination of the orientation vectors in the TD and ND. Thus, the orientation vector along the ND contributed to scattering [Fig. 2(b)].
3. T–MN orientation: The sample, as in Figure 2(a), was flipped so that the TD was

**Table II.** Film-Extrusion Conditions

| Blow-Up Ratio | Die Gap (mL) | Draw-Down Ratio | Die (in.) | Air Ring | Frost-Line Height (ZN; in.) | Lay Flat Width (in.) | Output (lb/h) | Screen Pack | Gauge (mL) |
|---|---|---|---|---|---|---|---|---|---|
| 2.5 | 60 | 19.2 | 4 | Standard | 9–14 | 14 | 75 | Standard | 1.25 |

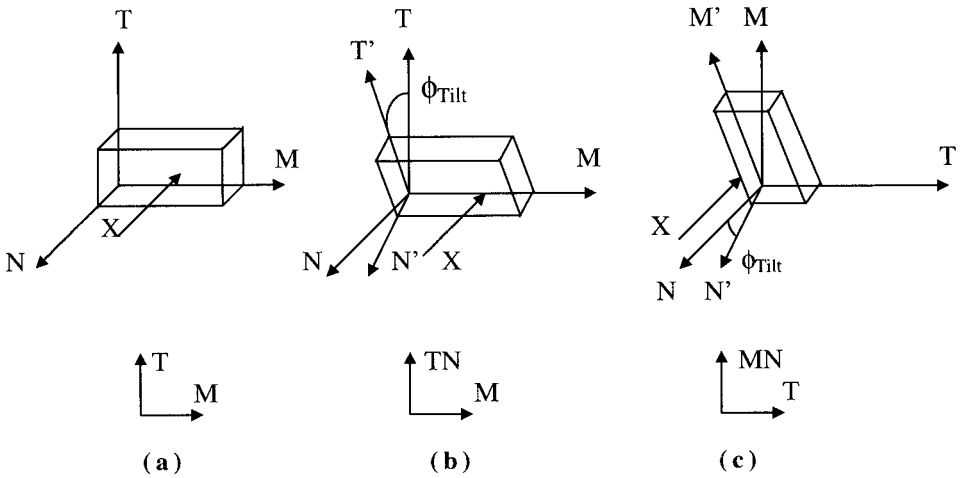


**Figure 2.** (a) M–T, (b) M–NT, and (c) T–MN orientations. The prime coordinates are after tilting; the unprimed coordinates are the original arrangement with the X-ray beam in the ND. Also shown are simple sketches of the orientation used in Figure 4 and the acronyms used in the text.

horizontal and the MD was vertical. It was rotated about the TD by 45° so that the orientation vector along the vertical axis was a combination of the orientation vectors along the MD and ND [Fig. 2(c)].

For the M–T projection, an azimuthal average yields the radial plot in Figure 3, showing intensity versus scattering vector $\mathbf{q} = 4\pi[\sin(\theta/2)]/\lambda$, where $\theta$ is the scattering angle and $\lambda$ is the wavelength. Least-squares fits with the Hoseman–

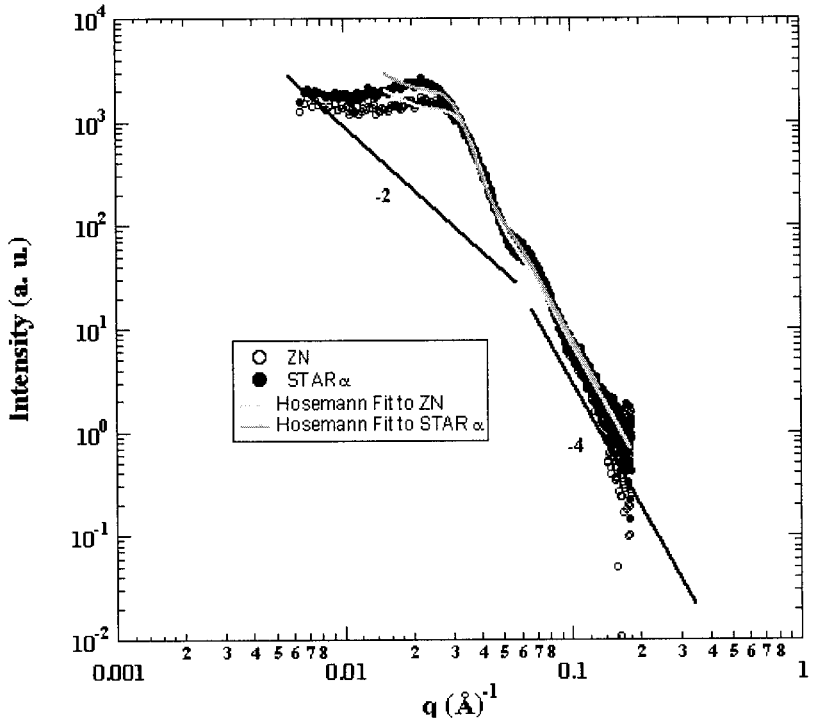


**Figure 3.** SAXS intensity (au) versus $\mathbf{q}$ $(\text{Å})^{-1}$ for STAR $\alpha$ and ZN samples in the M–T orientation [Fig. 2(a)]. Fits are to the Hoseman–Bagachi function.[15,16]

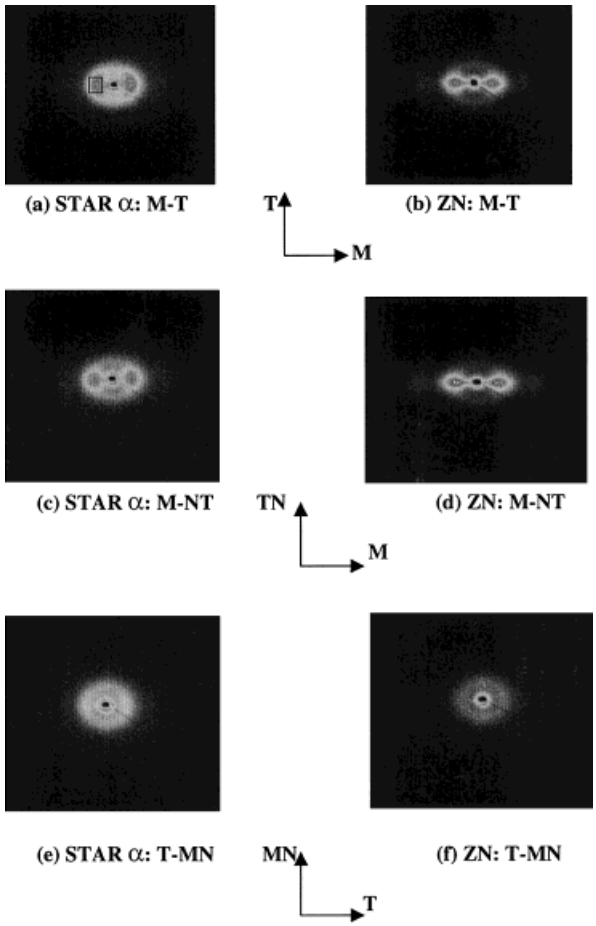


**Figure 4.** 2D SAXS patterns for the two samples in three different orientations. The weak lines pointing to the lower right corners are the transmission monitor wires.

Bagachi function[15,16] (shown in Fig. 3) indicate similar lamellar thicknesses and correlation distances for the films. Thus, the main difference on a nanometer scale is orientation, as seen in Figures 4 and 5. Azimuthal averages of M–NT and T–MN are essentially identical to those shown in Figure 3.

### *SAXS Analysis of 2D Orientation*

The SAXS measurements were conducted with the sample orientations shown in Figure 2 and with the nomenclature M–T, M–NT, and T–MN. Corrected 2D SAXS patterns are shown in Figure 4 for the three different orientations of the samples STAR $\alpha$ and ZN. The sample orientation is designated below each image with reference to Figure 2.

The observed orientation in the SAXS pattern is normal to the material orientation because it reflects a Fourier transform of real space. For instance, the sharp orientation of the SAXS pattern for ZN in Figure 4(b) along the MD indicates preferred lamellar orientation in the TD. The SAXS orientation describes the lamellar normal orientation in the indicated plane of projection.

Quantitatively, Figure 4(a,b) (M–T) and Figure 4(c,d) (M–NT) show that ZN has a higher degree of lamellar normal orientation along the MD than STAR $\alpha$. In Figure 4(b,d), a faint second-order peak can be seen at an intermediate angle (distance from the center).

Figure 4(e,f) presents 2D plots for STAR $\alpha$ and ZN, respectively, placed in orientation T–MN, as shown in Figure 2(c). In this case, both samples quantitatively show a much weaker orientation. This weak orientation for the T–MN projection can be explained by the 3D analysis presented later.

Averaging the data sets in the 2D plots (shown later in Fig. 7) about an azimuthal angle ($\phi$) produces a plot of intensity as a function of the azimuthal angle. The azimuthal plot is used to calculate $\langle\cos^2(\phi)\rangle$ for the projection through the calculation of the average cosine squared of the azimuthal angle weighted by the scattered intensity.[4] The azimuthal plots for the three positions of the samples are shown in Figure 5.

Because the peak in the SAXS pattern (Fig. 3) is related to the long period[15,16] and is associated with the lamellar ND, the azimuthal plots (Fig. 5) can be used to calculate the average cosine squared of the normal to the lamellae. This can be calculated under the assumption that the normal displays a uniaxial orientation[4] (i.e., the orientation is symmetric about a selected axis of the sample, such as in a fiber pattern, as in previous publications[2–4]) or by the consideration of two projections of the lamellar normal vector and calculation of the 3D orientation, as described here.

If it is assumed that the sample shows uniaxial orientation, the average cosine squared of the angle $\phi$ between the lamellar normal in projection and the chosen axis (MD) of uniaxial symmetry is calculated by integration and normalization of $I(\phi)\cos^2(\phi)\sin(\phi)$, where $\phi$ is the azimuthal angle in Figure 5.[4] The $\sin(\phi)$ term is used to reflect uniaxial symmetry (fiber symmetry). That is, as the azimuthal angle from the axis of orientation increases, the intensity from the observed plane must be multiplied by $\sin(\phi)$ to account for the increasing fraction of lamellae that do not fall in the plane of observation for SAXS.

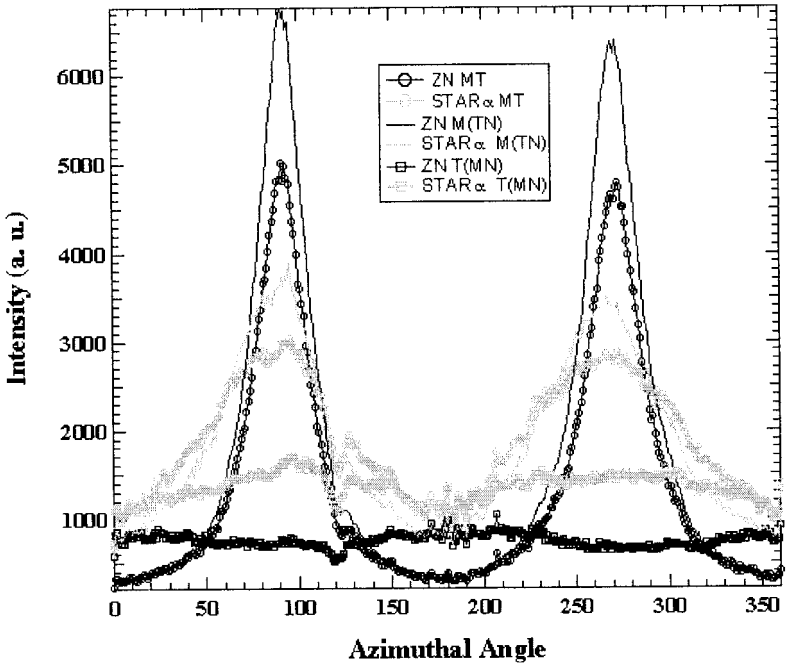


**Figure 5.** Azimuthal plot for the two samples in three orientations from Figures 2 and 4. Dark curves are ZN. The intensities are relative for a given sample because the same sample was used for different orientations.

If uniaxial orientation is not assumed, then the lamellar normal projected onto the plane of observation, that is, the M–T planar projection of the 3D orientation, $\langle\cos^2(\phi_{MT})\rangle$, can be calculated by integration of $I(\phi_{MT})\cos^2(\phi_{MT})$, with no $\sin(\phi_{MT})$ term.[4] Therefore,

$$\langle\cos^2(\phi_{MT})\rangle = \int_0^{360} I(\phi_{MT})\cos^2(\phi_{MT})d\phi_{MT} \Big/ \int_0^{360} I(\phi_{MT})d\phi_{MT} \quad (1)$$

where $\langle\cos^2(\phi_{MT})\rangle$ represents the M–T planar projection of the average normal to the lamellar plane in the MD direction (in Fig. 5, MD is at 90° for the M–T projection, so $\phi_{MT} = 0$ at 90°). $\langle\cos^2(\phi_{MT})\rangle$ can be used together with another planar projection such as $\langle\cos^2(\phi_{M-NT})\rangle$ or $\langle\cos^2(\phi_{T-MN})\rangle$ to determine the 3D orientation of the lamellar normal to the MD, TD, and ND represented by the angles $\phi_M$, $\phi_T$, and $\phi_N$, respectively.

### *SAXS Calculations*

The scattering vector **q** can be represented in three dimensions, as shown in Figure 6. **q** reflects the direction associated with an observed intensity. The direction of **q** at the maximum of a 2D scattering pattern is the same as the preferred direction of the lamellar normals in a 2D projection on the plane of observation.

From the calculations shown in the next two subsections, it is seen that, to determine the average angle of tilt of the lamellar normal with the MD, TD, and ND ($\phi_M$, $\phi_T$, and $\phi_N$), only two of the three orientations are needed. Two of these combinations are discussed later.

Figure 7 schematically shows the three observed projections and orientation angles ob-

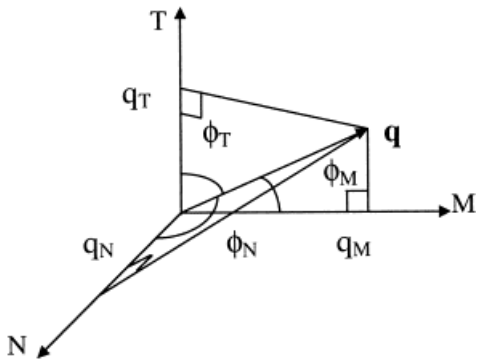


**Figure 6.** 3D view of the resultant scattering vector **q**.[17]

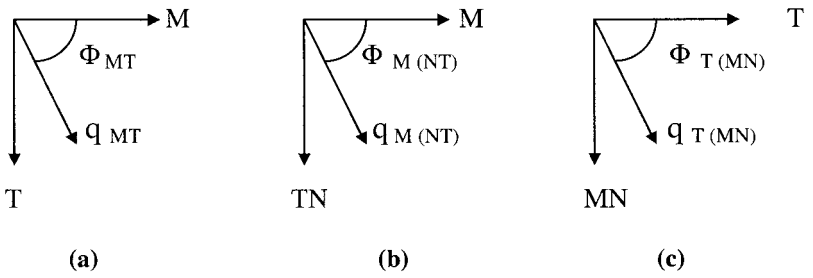


**Figure 7.** Direction of the intensity vector in three different orientations. $\Phi_{MT}$ is the angle made by scattering vector **q** with the horizontal (MD) when projected onto the M–T plane, $\Phi_{M(NT)}$ is the angle made by **q** with the horizontal (MD) when projected onto the M–NT plane, and $\Phi_{M(NT)}$ is the angle made by **q** with the horizontal (TD) when projected onto the T–MN plane.

tained from Figure 5 with eq 1. The two calculations of $\phi_M$, $\phi_T$, and $\phi_N$ are described next.

*Case 1.* M–T and M–NT Orientation.

From Figures 6 and 7(a),

$$q_M = q_{MT}\cos\,\phi_{MT} \tag{2}$$

$$q_T = q_{MT}\sin\,\phi_{MT} \tag{3}$$

From eqs 1 and 2,

$$q_T/q_M = \tan\,\phi_{MT} \tag{4}$$

For M–NT orientation [Fig. 7(b)], the sample is tilted across the MD by an angle $\phi_{Tilt}$ (in our case, $\phi_{Tilt} = 45°$), so the scattering vector in the vertical direction will have a component of orientation along the TD and a component of orientation along the ND. From Figures 6 and 7(b),

$$-q_N\sin\,\phi_{Tilt} + q_T\cos\,\phi_{Tilt} = q_{M(NT)}\sin\,\phi_{M(NT)}. \tag{5}$$

$$q_M = q_{M(NT)}\cos\,\phi_{M(NT)} \tag{6}$$

From eqs 4–6,

$$q_N/q_M = [(\tan\,\phi_{MT}/\tan\,\phi_{Tilt}) - (\tan\,\phi_{M(NT)}/\sin\,\phi_{Tilt})] \tag{7}$$

$$q_N/q_T = [1/\tan\,\phi_{MT}]/[(\tan\,\phi_{MT}/\tan\,\phi_{Tilt}) - (\tan\,\phi_{M(NT)}/\sin\,\phi_{Tilt})] \tag{8}$$

From Figure 6,

$$\cos^2\phi_M = q_M^2/q^2 = q_M^2/(q_M^2 + q_T^2 + q_N^2) \tag{9}$$

$$\cos^2\phi_T = q_T^2/q^2 = q_T^2/(q_M^2 + q_T^2 + q_N^2) \tag{10}$$

$$\cos^2\phi_N = q_N^2/q^2 = q_N^2/(q_M^2 + q_T^2 + q_N^2) \tag{11}$$

Substituting eqs 4, 7, and 8 into eqs 9–11 and substituting $A = (\tan\,\phi_{(MT)})$ and $B = [(\tan\,\phi_{MT}/\tan\,\phi_{Tilt}) - (\tan\,\phi_{M(NT)}/\sin\,\phi_{Tilt})]$, we get

$$\cos^2\phi_M = 1/\{1 + A^2 + B^2\} \tag{12}$$

$$\cos^2\phi_T = A^2/\{1 + A^2 + B^2\} \tag{13}$$

$$\cos^2\phi_N = B^2/\{1 + A^2 + B^2\} \tag{14}$$

Values of $\phi_{M(NT)}$ and $\phi_{(MT)}$ obtained from Figure 5, on substitution into eqs 12–14, give the values of $\langle\cos^2\,\phi_M\rangle$, $\langle\cos^2\,\phi_T\rangle$, and $\langle\cos^2\,\phi_N\rangle$ reported in Table III. From Figure 7, it is clear that

$$\langle\cos^2\phi_M\rangle + \langle\cos^2\phi_N\rangle + \langle\cos^2\phi_T\rangle = 1 \tag{15}$$

Equation 15 can be used to crosscheck the values in Table III.

*Case 2.* M–T and T–MN Orientation.

For the M–NT orientation [Fig. 7(c)], the sample is tilted across the TD by an angle $\phi_{Tilt}$ (in our case, $\phi_{Tilt} = 45°$), so the scattering vector in the vertical direction will have a component of orientation along the MD and a component of orientation along the ND. From Figures 6 and 7(c),

$$q_N/q_M = 1/\tan\,\phi_{Tilt} - (\tan\,\phi_{(MN)T})(\tan\,\phi_{(MT)})/(\sin\,\phi_{Tilt}) \tag{16}$$

**Table III.** Values of the Cosine Squared of Angles Made by the Scattering Vector with the MD, TD, and ND

| Sample | | STAR $\alpha$ | ZN |
|---|---|---|---|
| Calculated projections for case 1 (case 2) | $\langle\cos^2 \phi_M\rangle$ | 0.596 (0.610) | 0.773 (0.756) |
| | $\langle\cos^2 \phi_T\rangle$ | 0.379 (0.388) | 0.207 (0.202) |
| | $\langle\cos^2 \phi_N\rangle$ | 0.025 (0.002) | 0.020 (0.045) |
| | Sum | 1.000 (1.000) | 1.000 (1.003) |
| Observed projections for SAXS (SALS) data | $\langle\cos^2 \phi_{TM}\rangle$ | 0.611 (0.540) | 0.789 (0.600) |
| | $\langle\cos^2 \phi_{M(NT)}\rangle$ | 0.666 | 0.813 |
| | $\langle\cos^2 \phi_{T(MN)}\rangle$ | 0.534 | 0.477 |

$$q_N/q_T = [1/\tan \phi_{(MT)}][1/\tan \phi_{Tilt} - (\tan \phi_{(MN)T})(\tan \phi_{(MT)})/(\sin \phi_{Tilt})] \quad (17)$$

Substituting eqs 4, 16, and 17 into eqs 9–11 and $A = (\tan \phi_{(MT)})$ and $C = [1/\tan \phi_{Tilt} - (\tan \phi_{(MN)T})(\tan \phi_{(MT)})/(\sin \phi_{Tilt})]$, we get

$$\cos^2 \phi_M = 1/(1 + A^2 + C^2) \quad (18)$$

$$\cos^2 \phi_T = A^2/(1 + A^2 + C^2) \quad (19)$$

$$\cos^2 \phi_N = C^2/(1 + A^2 + C^2) \quad (20)$$

Values of $\phi_{(MN)T}$ and $\phi_{(MT)}$ obtained from Figure 5, on substitution into eqs 18–20, give the values of $\langle\cos^2 \phi_M\rangle$, $\langle\cos^2 \phi_T\rangle$, and $\langle\cos^2 \phi_N\rangle$ reported in Table III (parenthetic values). The results from case 2 can be used to crosscheck those obtained from case 1.

### Results from Biaxial Orientation Calculations

The results in Table III show that both cases give similar results. The sum of $\langle\cos^2 \phi\rangle$ is also shown, which is close to 1. The average cosine squared projection of the lamellar normals from the $i$ axis, $\langle\cos^2 \phi_i\rangle$, can be used in a Wilchinsky triangle[18–20] construction for the average lamellar normal orientation (Fig. 8). This ternary plot seems the simplest for displaying the direction of the lamellar orientation for these samples. We construct the Wilchinsky triangle[18–20] by counting from the opposite side of a direction $i$ the value of $\langle\cos^2 \phi_i\rangle$ and making a point where the three $\langle\cos^2 \phi_i\rangle$ values intersect (according to eq 15). For a randomly oriented sample, $\langle\cos^2 \phi_M\rangle = \langle\cos^2 \phi_N\rangle = \langle\cos^2 \phi_T\rangle = 1/3$, and a point in the center of the Wilchinsky triangle results. For perfect orientation in the MD, a point at the MD corner results. Orientation of the lamellar normals in the M–T plane occurs for a point on the bottom axis.[18–20]

The Wilchinsky plot shows that the lamellae lie with the normal basically in the MT plane with stronger orientation in the MD direction. The lamellae are essentially perpendicular to the film surface in both cases. ZN has a higher lamellar normal orientation in the MD.

The T–MN projection in Figure 4 shows little orientation (bottom two patterns). This can be understood in the context of the Wilchinsky diagram if we draw a line from the TD to the middle of the ND–MD axis through the random point. Projecting the ZN and STAR $\alpha$ point along a line parallel to the ND–MD axis shows close to random orientation for the T–MN projection of ZN, as observed in Figure 4. A similar construction for M–NT shows a strong deviation from the random point consistent with Figure 4.

### Transmission Optical Microscopy Analysis

Transmission optical micrographs are shown in Figure 9. The images are dominated, especially for the ZN film, by surface features when observed in air. When the same film is immersed in an index-matching fluid, the bulk structure can be observed, as shown in Figure 1. Benzyl alcohol ($n \sim 1.52$) has a refractive index almost the same as that of polyethylene ($n \sim 1.49$–$1.51$), as seen in Figure 1(b).

Under crossed polars in the optical micrographs of Figure 9, birefringent regions are white. We associate these birefringent regions with micrometer-scale crystalline domains, whereas the dark regions reflect amorphous regions.

The ZN film shows well-organized linear structures in both surface and bulk micrographs. The linear structures for the ZN film are in the MD. STAR $\alpha$ shows disorganized domains in both mi-

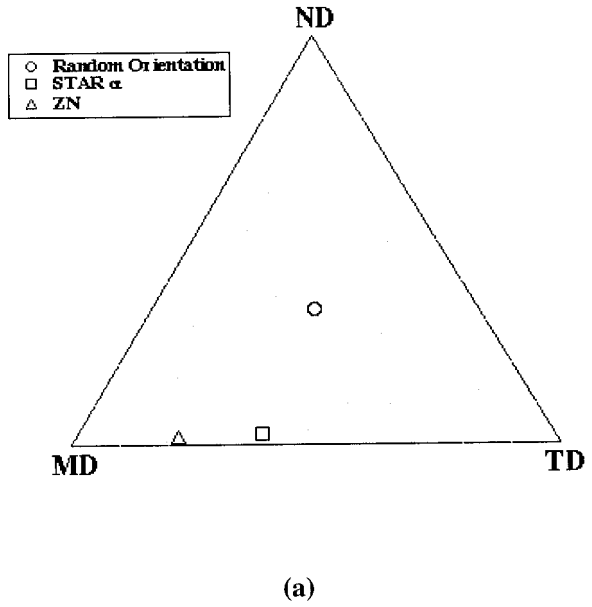


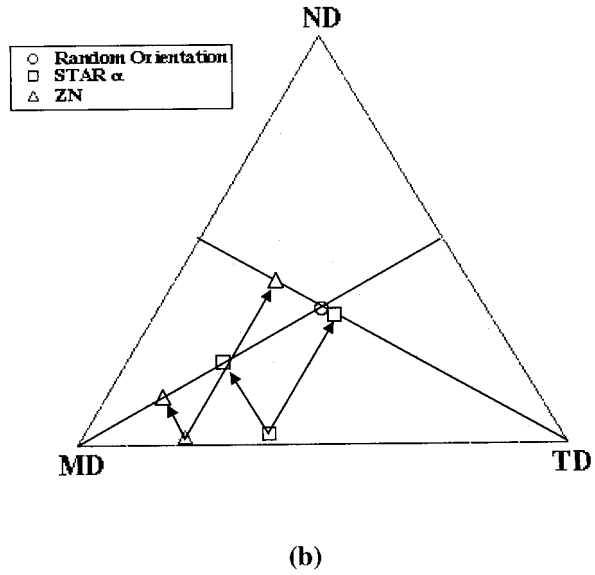


**Figure 8.** (a) Wilchinsky triangle[18–20] for the average lamellar normal orientation of a completely randomly oriented sample (central dot) and the two samples examined here. ZN has stronger lamellar normal orientation in the MD. (b) Measured projections as seen on Wilchinsky triangle planar projections showing close to random orientation for T–MN (as seen in Fig. 4) and higher orientation for M–TN than for MT. The line bisecting the M–N plane is the T–MN plane, whereas the line bisecting the N–T plane is the M–NT plane. Arrows indicate the direction of projections on the T–MN and M–NT planes.

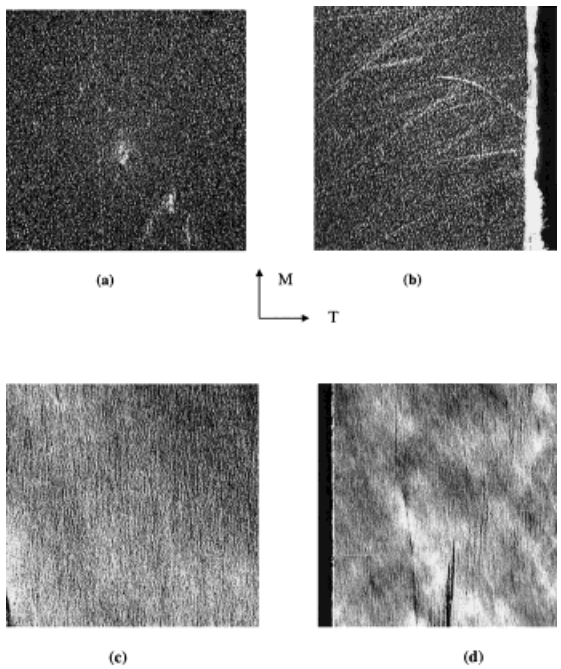


**Figure 9.** Optical micrographs of the two films (original magnification, 400×) under crossed polars: (a) STAR $\alpha$ in air (surface), (b) STAR $\alpha$ immersed in benzyl alcohol (bulk), (c) ZN in air (surface), and (d) ZN immersed in benzyl alcohol (bulk).

crographs, with a few rodlike structures of unknown origin at an angle to the MD in the bulk micrograph.

The optical micrographs support micrometer-scale orientation as the main difference between the two films. The micrographs may also support stacked lamellar morphology in ZN, as discussed later.

## SALS

Single sheets of blown films were immersed in benzyl alcohol, an index-matching liquid, to remove surface scattering. In the absence of an index-matching solvent, the ZN film was too turbid for the laser beam to pass through, making light scattering from the film impossible. The films attained comparable clarity when immersed in benzyl alcohol, as seen in Figure 1(b). Light scattering measurements were conducted with a helium neon laser with a 0.6328-$\mu$m wavelength and pinhole optics. The SALS pattern was projected onto a screen and imaged with a charge couple device (CCD) camera equipped with a macrolens, as previously reported.[14] Scattering was corrected for a benzyl alcohol background, dark

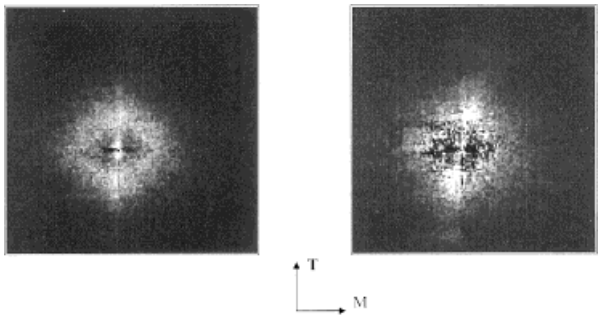


**Figure 10.** 2D corrected SALS patterns for STAR $\alpha$ (left) and ZN (right) films. A correlation peak associated with regular spacing of linear birefringent regions appears as a ring in the patterns. The MD is roughly in the horizontal plane, with the bright lobes normal to MD.

current, and sensitivity of the detector. All scattering was run with no polarizers other than the inherent polarization of the laser source. The MD direction of the samples is roughly in the horizontal direction of the SALS pattern in Figure 10, with the bright peaks in Figure 10 oriented normal to the MD, which is consistent with the optical micrographs.

The 2D patterns display different degrees of orientation in SALS, with the ZN sample showing stronger orientation in the MD direction (bright peaks normal to MD). The difference in orientation parallels that seen in the SAXS pattern despite a difference in size of roughly 3 orders between SALS and SAXS. The SAXS M–T orientation [Fig. 4(a)] is orthogonal to the SALS orientation shown in Figure 10. SAXS, SALS, and optical microscopy indicate that lamellae stacked within the rodlike structures of Figure 9 are normal to the fiber axis, which is consistent with stacked lamellar morphologies.[21–23]

The corrected SALS patterns shown in Figure 10 were averaged about the beam center, resulting in the one-dimensional (1D) radial scattering patterns shown in Figure 11. The SALS 1D patterns show a correlation peak associated with the ring seen in Figure 10. The correlation size, $2\pi/\mathbf{q}^*$, is about 1.5 $\mu$m, with the ZN film showing a slightly larger spacing. A Guinier fit is done on the curves at the weak knee seen at high $\mathbf{q}$, resulting in a radius of gyration ($R_g$) that is converted to the width of the lines ($W$) seen in the optical micrographs by $W = 2R_g$. The region lower

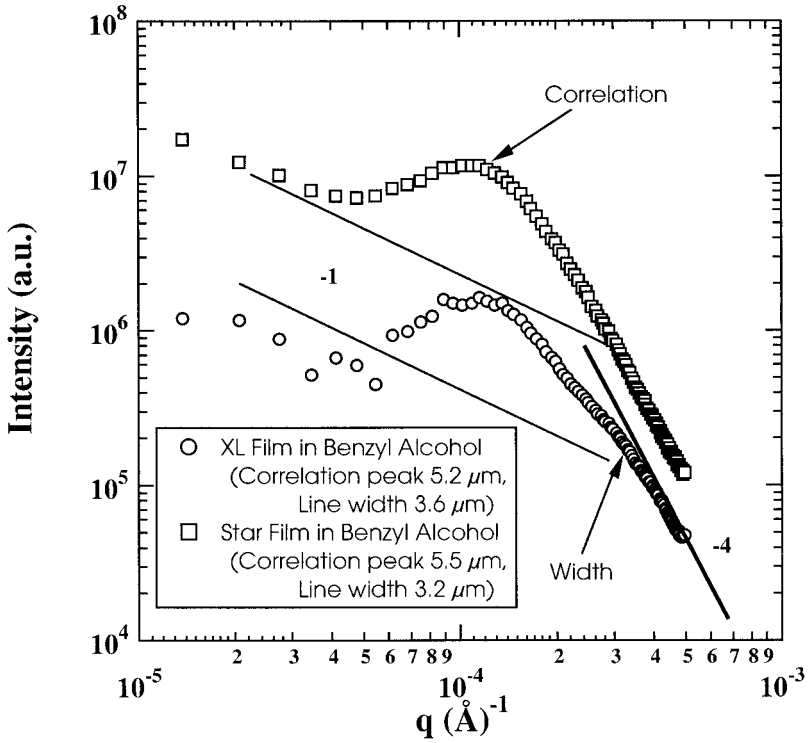


**Figure 11.** Average 1D intensity versus scattering vector $\mathbf{q} = 4\pi/[\lambda \sin(\theta/2)]$. The peak in the pattern corresponds to the ring seen in Figure 10. Correlation distances and line widths are noted as described in the text.

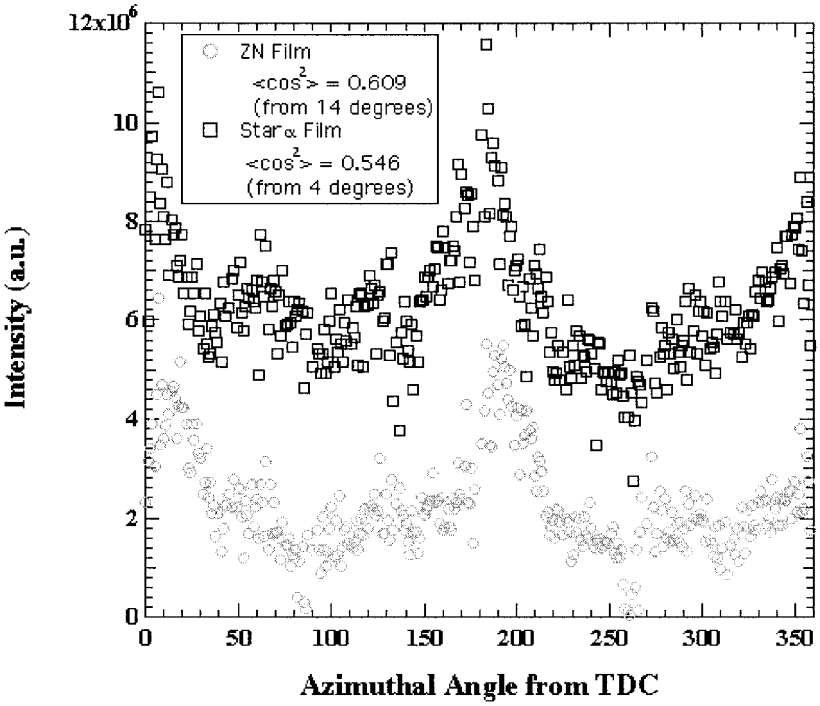


**Figure 12.** Radial plot of intensity versus radial angle for the two films. The average cosine squared for the M–T planar projection is shown in the inset.

in **q** than the weak knee is consistent with 1D objects, as indicated by a superimposed power-law decay of about −1 slope in the log–log plot of Figure 11. At high **q**, a Porod regime of −4 slope is seen, indicating sharp interfaces to the linear domains.

The average cosine squared for the SALS patterns can be obtained in a fashion similar to that for SAXS for the M–T planar projection. The radial plot of intensity near the peak is shown in Figure 12. From this plot, the average cosine squared for the M–T projection can be calculated (ZN, 0.609; STAR $\alpha$, 0.546), which is consistent, although of lower value, with the values reported for SAXS for the lamellar structure in the M–T plane (Table III). This supports a hierarchical structure for the rodlike structures seen in the optical micrographs (Fig. 9), with orientation being stronger on a nanoscale and becoming more disorganized on larger scales.

## DISCUSSION

### MWD and Orientation

The ZN film was manufactured from HDPE synthesized with a Ziegler–Natta catalyst, whereas the STAR $\alpha$ film was manufactured from HDPE synthesized with a single-site catalyst. Ziegler–Natta catalysts give HDPE with a broader MWD compared with that obtained from single-site catalysts[1] (Table I). From the SAXS and SALS analyses, it can be seen that the ZN film has a higher degree of orientation than the STAR $\alpha$ film. This variation in orientation could be related to the MWD. A broader distribution contains more high molecular weight chains. The presence of long chains increases the number of chain entanglements. Hence, ZN is expected to display a longer relaxation time and a higher orientation due to chain entanglements. Thus, the ZN film, with a broader MWD, should show more oriented lamellar structures with maximum chain orientation in the direction of maximum strain, which can be estimated from the blow-up and the draw-down ratios (Table I) to be $\cos^2 \phi_{MT} = 0.98$. Because the chains pack in the direction of the lamellar normal, this indicates lamellar normal orientation in the MD also. The relaxation time and time of application of strain in the film-blowing process in ZN lead to $\cos^2 \phi_{MT} = 0.79$ and in STAR $\alpha$ lead to $\cos^2 \phi_{MT} = 0.61$. The results obtained from the SAXS and SALS analyses are consistent with this model.

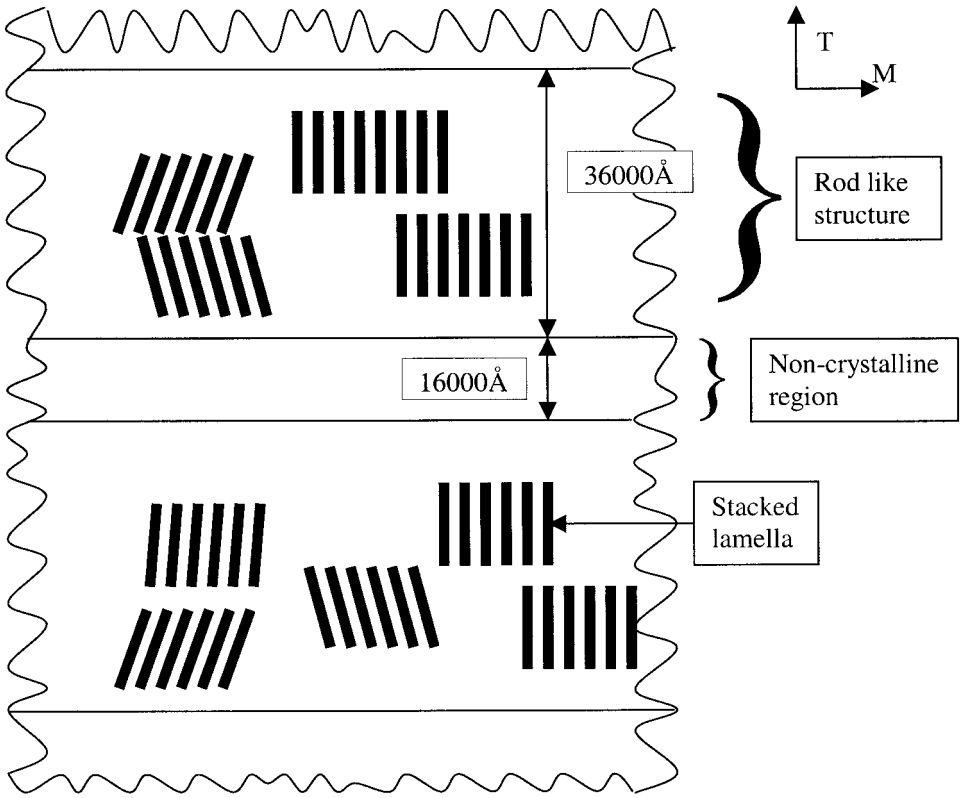


**Figure 13.** Schematic of the morphological features observed for the STAR $\alpha$ and ZN films. Lamellae are not drawn to scale and are smaller than shown. The orientation of the micrometer scale is lower than the lamellae.

### Relation between Micrometer-Scale and Nanometer-Scale Orientation

The micrometer-scale orientation of linear domains seen in Figures 9, 10, and 12 is normal to the lamellar orientation seen in Figures 3 and 4. The lamellar domains from SAXS are about 120 Å thick with a long period spacing of about 170 Å. The linear domains are about 3.6 $\mu$m (36,000 Å) wide and are spaced regularly at about 1.6$\mu$m (16,000 Å) from SALS. The SALS results bring up two main questions: (1) what governs the regularity of the linear domain spacing and 2) why are the linear domains orthogonal to the lamellar domains? The second question might be answered by the consideration of the possibility of stacked lamellar structures within the linear domains seen in light scattering and optical microscopy. These stacked lamellar structures have been observed in blown and oriented HDPE films and are composed of around 3–10 lamella stacked together in blocks.[21–24] The lamellae in these stacked lamellar structures are typically oriented with the basal planes almost perpendicular to the MD–TD plane and their surface normals parallel to the MD. Such stacked lamellar structures are shown in the schematic diagram in Figure 13 and depicted as composing the primary units of the linear structures observed in the optical data. The structure in Figure 13 explains the orthogonal relationship between the lamellae observed in the SAXS data and the linear structures observed in the SALS data. The ratio in size between the lamellar thickness and the linear width is about 2 orders. One should consider that the linear domains are composed of many stacked lamellar structures across their width, rather than a single cylindrite structure.

The regularity in lateral spacing of the linear domains is a far more puzzling question. A high degree of order is necessary to produce the correlation peaks seen in Figures 11 and 12. Such order is often due to a balance between thermodynamics and kinetics, such as for spinodal decomposition. Keith and Padden[25] considered a possible relationship between the transport of impurities or noncrystallizable chains and the la-

mellar growth rate as an explanation for coarsening in spherulitic crystallites through the del parameter, $\delta = D/G$, where $D$ is the diffusion coefficient for noncrystallizable chains or species and $G$ is, in this case, the lateral growth rate for lamellae in the linear structures. The origin of the regularly spaced linear structure observed in the optical data, therefore, could be explained by the buildup of noncrystallizable species in the regions between the crystalline material. The resin with higher impurities, that is, low molecular weight polyethylene or branched chains, is likely to show a stronger tendency to form an ordered fibrillar structure under this line of reasoning. This could explain the ZN sample showing strong rodlike structures.

A second potential explanation is the spinodal mode of crystallization, such as discussed by Strobl.[26] In this model, the phase separation of species differing in molecular weight or branch content precedes crystallization under the stresses of the film-blowing operation. Some evidence for the spinodal mode exists from SAXS studies made by Schultz et al.[27] on melt-crystallized polypropylene films. The observed micrometer-scale correlation is consistent with sizes expected from spinodal decomposition.

### Film Clarity

The ZN film was cloudy, whereas the STAR $\alpha$ film was transparent and glossy. Both films were blown under similar conditions. Both films were transparent on extrusion, but the ZN film turned hazy at a well-defined frost line. These films had the same degree of crystallinity and almost identical lamellar structures and sizes. The primary structural factor that varied between the films was the degree of orientation on both the nanometer and micrometer scales. Wilkes et al.[1] indicated that surface roughness is associated with haze in HDPE films. We verified this with index matching and optical microscopy. In the blown films discussed here, the surface structure and bulk structure appear to be related, as shown in Figure 9. The rodlike structures of Figure 9 appear to be intimately related to the bulk crystalline morphology on the nanometer to micrometer scales. Our data indicate that this structure is consistent with a stacked lamellar morphology.[21–23] Figure 13 shows a schematic of the regular arrangement of the stacked lamellar structures associated with surface roughness and haze. In Figure 13, the sizes are not relative, and the orientation of the micrometer scale is weaker than the lamellae.

From the SALS, SAXS, and optical microscopy measurements, the surface irregularities and bulk orientation on the micrometer scale appear to be linked. The surface haze is tied to a hierarchical structure composed of nanometer-scale oriented stacked lamellar morphologies that cluster into oriented micrometer-scale, rodlike structures governed by Keith and Padden's transport/growth rate laws or spinodal mode morphological development. These oriented and correlated micrometer-scale domains lead to surface roughness in highly oriented systems.

## CONCLUSION

Two blown films were studied in this work: a ZN film manufactured from HDPE synthesized with a Ziegler–Natta catalyst and a STAR $\alpha$ film manufactured from HDPE synthesized with a single-site catalyst. The ZN film exhibited high haze, whereas the STAR $\alpha$ film was relatively clear. Both films were blown under similar conditions. Both films were transparent on extrusion, but the ZN film turned hazy at a well-defined frost line. Both the ZN and STAR $\alpha$ films had similar lamellar structures. The primary difference between the films was the degree of orientation, that is, the orientation of the lamellar structures on a nanometer scale. The lamellar orientation was determined by SAXS. The ZN film had lamellae regularly arranged and oriented with normals along the film MD. The ZN film also exhibited rodlike structures on the surface, oriented along the film MD on a micrometer scale. The micrometer-scale characteristics were determined by SALS and optical microcopy. The lamellar orientation was linked to the formation of micrometer-scale, rodlike structures, which produced roughness on the surface of the film. These surface irregularities scattered light and were the cause of the haze observed in the ZN film. The lamellar structure and size of the STAR $\alpha$ film were very similar to those of the ZN film, but there was lower orientation. The STAR $\alpha$ film exhibited much less surface roughness with respect to the ZN film and was relatively clear because of lower lamellae and associated micrometer-scale orientation.

A new approach to the analysis of 3D lamellar orientation from SAXS was also presented. The approach takes advantage of the Wilchinsky con-

struction to simplify the comparison of bulk orientation.

## REFERENCES AND NOTES


1. Johnson, M. B.; Wilkes, G. L.; Sukhadia, A. M.; Rohlfing, D. C. J Appl Polym Sci 2000, 77, 2845.
2. Hughes, O. R.; Kurschus, D. K.; Saw, C. K.; Flint, J.; Bruno, T. P.; Chen, R. T. J Appl Polym Sci 1999, 74, 2325.
3. Murthy, N. S.; Grubb, D. T.; Zero, K. Macromolecules 2000, 33, 1012.
4. Prasad, A.; Shroff, R.; Rane, S.; Beaucage, G. Macromolecules 2001, 42, 3103.
5. Jianjun, L.; Hung-Jue, S. J Mater Sci 2000, 35, 5169.
6. Krishnaswamy, R. K.; Sukhadai, A. M. Polymer 2000, 41, 9205.
7. Yong-Man, K.; Jung-Ki, P. J Appl Polym Sci 1996, 61, 2315.
8. Stehling, F. C.; Speed, C. S.; Westerman, L. Macromolecules 1981, 14, 698.
9. Hashimoto, T.; Todo, A.; Murakami, Y. J Polym Sci Polym Phys Ed 1977, 15, 501.
10. Kojima, M.; Magill, J. H.; Lin, J. S.; Magonov, S. N. Chem Mater 1997, 9, 1145.
11. Samuels, R. J. J Polym Sci Polym Phys Ed 1969, 7, 1197.
12. Pinto, G.; Larena, A. Polym Eng Sci 1993, 33, 742.
13. Haudin, J. M.; Piana, A.; Monasse, G.; Monge, B.; Gourdan, B. Ann Chim Sci Mater 1999, 24, 555.
14. Hyeon-Lee, J.; Guo, L.; Beaucage, G.; Antonieta Macip-Boulis, M.; Arthur, J. M.; Yang, A. J Polym Sci Polym Phys Ed 1996, 34, 3073.
15. Roe, R. J. Methods of X-Ray and Neutron Scattering in Polymer Science; Oxford University Press: New York, 2000; p 199.
16. Hoseman, R.; Bagachi, S. N. Direct Analysis of Diffraction by Matter; North Holland: Amsterdam, 1962; p 410.
17. Roe, R. J. Methods of X-Ray and Neutron Scattering in Polymer Science; Oxford University Press: New York, 2000; p 119.
18. Alexander, L. E. X-Ray Diffraction Methods in Polymer Science; Krieger: Malabar, FL, 1985; pp 245–258.
19. Wilchinsky, Z. W. J Appl Polym Sci 1963, 7, 923.
20. Wilchinsky, Z. W. J Appl Phys 1959, 30, 792.
21. Tagawa, T.; Ogura, K. J Polym Sci Polym Phys Ed 1980, 18, 971.
22. Kim, Y.; Kim, C.; Park, J.; Kim, J.; Min, T. J Appl Polym Sci 1996, 61, 1717.
23. Kim, Y.; Kim, C.; Park, J.; Lee, C.; Min, T. J Appl Polym Sci 1997, 63, 289.
24. Hobbs, J. K.; Miles, M. J. Macromolecules 2001, 34, 353.
25. Keith, H. D.; Padden, F. J. J Appl Phys 1964, 35, 1270, 1286.
26. Strobl, G. The Physics of Polymers, 2nd ed.; Springer-Verlag: Berlin, 1997; p 173.
27. Schultz, J. M.; Lin, J. S.; Hendricks, R. W. J Polym Sci Polym Phys Ed 1981, 19, 609.